Hindawi
Adsorption Science & Technology
Volume 2022, Article ID 5628032, 13 pages
https://doi.org/10.1155/2022/5628032

Research Article

ATO/Polyaniline/PbS Nanocomposite as Highly Efficient Photoelectrode for Hydrogen Production from Wastewater with Theoretical Study for the Water Splitting

Mohammed A. H. Khalafalla,[1] **N. M. A. Hadia**,[2,3] **Asmaa M. Elsayed**,[4] **Mansoor Alruqi**,[5] **Wassim El Malti**,[6] **Mohamed Shaban**,[4] **and Mohamed Rabia**[4,7]

[1]*Taibah University, Faculty of Science, Department of Physics, Yanbu Branch, Yanbu, Saudi Arabia*
[2]*Physics Department, College of Science, Jouf University, Al-Jouf, Sakaka, P.O. Box 2014, Saudi Arabia*
[3]*Basic Sciences Research Unit, Jouf University, Al-Jouf, Sakaka, P.O. Box 2014, Saudi Arabia*
[4]*Nanophotonics and Applications Lab, Physics Department, Faculty of Science, Beni-Suef University, Beni-Suef 62514, Egypt*
[5]*Department of Mechanical Engineering, College of Engineering, Shaqra University, Al Riyadh 11911, Saudi Arabia*
[6]*College of Engineering and Technology, American University of the Middle East, Kuwait*
[7]*Nanomaterials Science Research Laboratory, Chemistry Department, Faculty of Science, Beni-Suef University, Beni-Suef 62514, Egypt*

Correspondence should be addressed to N. M. A. Hadia; nmhadia@ju.edu.sa and Wassim El Malti; wassim.elmalti@aum.edu.kw

Received 22 May 2022; Revised 6 July 2022; Accepted 25 July 2022; Published 16 August 2022

Academic Editor: Adrián Bonilla-Petriciolet

Polyaniline-assisted deposition of PbS is carried out on antimony tin oxide (ATO) glass for ATO/PANI/PbS composite formation. The deposition of PbS was carried out inside and outside the polymer chains using the ionic adsorption deposition process. Various analyses were conducted to confirm the chemical structure and morphological, optical, and electrical properties of the resulting composite. TEM and SEM analyses demonstrated the spherical shape of PbS particles inside and outside the PANI network with more dark or white color, respectively. Moreover, the ImageJ program confirmed the composite formation. The XRD characterization showed the shifts in the PANI peaks after the composite formation with the appearance of a new additional peak related to PbS nanoparticles. The optical analyses were massively enhanced after the composite formation with more broadening in the Vis region at 630 nm, in which there was more enhancement in the bandgap that reached 1.5 eV. The electrode application in the H_2 generation process was carried out from wastewater (sewage water, third treatment) without any additional sacrificing agent. The electrode responded well to light, where the current density (J_{ph}) changed from 10^{-6} to 0.13 mA.cm^{-2} under dark and light, respectively. The electrode had high reproducibility and stability. The numbers of generated H_2 moles were 0.1 mmol/cm^2.h. The produced ΔH^* and ΔS^* were 7.3 kJ/mol and 273.4 J/mol.K, respectively. Finally, the mechanism explains the H_2 generation reaction using three-electrode cell.

1. Introduction

The increasing energy demand prompted research in different laboratories to work on renewable energy sources such as windmills and solar energy [1–4]. These sources can prevent the problem of nonrenewable energy sources in which the combustion of fossil fuels has a fetal effect on plants, animals, humans, and the environment. The combustion of fossil fuels produces harmful gases, such as CO_X, NO_X, and SO_X [5–7].

The water-splitting reaction producing hydrogen is a type of solar energy source that depends directly on sunlight. This reaction can be carried out as photochemical or photoelectrochemical. The water-splitting reaction generates hydrogen and

oxygen gases at the working and counter electrodes, respectively. This reaction can also help valorize the wastewater streams produced by the industrial, domestic, and agricultural activities worldwide, noting that enhancing the water quality belongs to one of the UN sustainable development goals (SDG #6) to be achieved by 2030. The splitting reaction requires semiconductor materials such as oxides, nitrides, and sulfides [8, 9]. Nevertheless, semiconductor polymers are the new category of photocatalytic materials used for this purpose having many advantages such as low cost, high quantum yield, large surface area, and easy preparation [10–16]. Polymer production is the replaceable category for all metal sources, especially in electronic devices. The researchers' primary aim in optimizing polymer preparation is to enhance the optical properties and reach the general optimum bandgap of 1.2 to 1.5 eV. This optimization is generally carried out by controlling the nanoscale and composite formation with additive materials possessing high optical efficiency [17].

Polyaniline and its derivatives represent one of the main polymers described. This category of polymers has additional benefits such as high compatibility, stability, porosity, safety, low cost, redox state, and low bandgap [18, 19].

Furthermore, PbS has a unique property in which the bandgap is in the range of 0.92 to 1.6 eV, depending on the size, with its black color that can trap the photons. PbS has additional electrical properties that qualify it for various applications in the renewable energy field, such as solar cells, optoelectronics, and water splitting [20, 21].

Recently, few studies included the application of polyaniline (PANI) and its derivatives in water-splitting reactions. Corte et al. [22] fabricated Ni/PANI composite and used it for water splitting from 0.5 M H_2SO_4 under artificial light. Belabed et al. [23] prepared PANI/TiO_2 for water splitting using artificial light (200 W tungsten lamp). In addition, Zhang et al. [24] synthesized PANI/MoS_2 for H_2 generation from an H_2SO_4 solution. All of the mentioned studies still suffer from the low H_2 quantity produced and low cell efficiency; sometimes, the efficiency is not even reaching 2%. Moreover, the previous studies usually use sacrificing agents to get the hydrogen gases, which cause electrode corrosion. Also, the previous studies used freshwater as a source of H_2 gas, with the stinginess of this freshwater for drinking, especially in water-poor countries [25–27]. In addition, most of the previous studies used high complexed devices for the deposition of metal oxides or sulfides. These devices require more time for deposition using chemical or physical vapor deposition, laser, wet spinning, and RF sputtering techniques [28, 29].

This study provides a renewable energy source (hydrogen gas fuel) by solving many previously described drawbacks and represents an opportunity to valorize wastewater. We used the PANI-assisted deposition for PbS nanocomposite through the polymer-assisted ionic adsorption method. The large surface area and porosity of PANI helped in the PbS deposition. The deposition process of polymer composite was carried out on ATO glass, in which the ATO/PANI/PbS composite was formed. The low-cost ATO/PANI/PbS nanocomposite was implemented as a working photocathode in a three-electrode cell for H_2 generation from wastewater (three-stage treatment sewage water) without any sacrificing agent under a solar simulator device (xenon lamp). The effect of light wavelength, light intensity, on/off chopped light, and the temperature was examined. The stability and mechanism of the electrode were mentioned and discussed.

2. Materials and Methods

2.1. Materials. Aniline and $(NH_4)_2S_2O_8$ were purchased from Rankem (India) and Winlab, respectively. Dimethyl sulfoxide (DMSO) was purchased from Sigma-Aldrich, USA. Acetic acid (CH_3COOH), $Pb(NO_3)_2$, iodine (I_2), and KI were purchased from El-Naser company, Egypt. Sewage water with the third treatment stage was obtained from the drinking water and sanitation company, Beni Suef City, Egypt.

2.2. Preparation of PANI/PbS Nanocomposites. PANI was prepared through the in situ oxidation polymerization method on antimony tin oxide (ATO) glass. Aniline (0.1 M) was dissolved in 0.5 M CH_3COOH under ultrasonic effect; in the same manner, 0.15 M $(NH_4)_2S_2O_8$ (oxidant) was dissolved. Then, the oxidant was added suddenly over the aniline solution in the presence of ATO glass. After 1 h, a complete precipitate was formed from PANI over ATO glass. The resulting ATO/PANI was dried at 60°C for 6 h.

The preparation of PbS was carried out by the chemical bath deposition process. 0.05 M $Pb(NO_3)_2$ was dissolved well at 60°C. Also, 0.01 M thiourea was dissolved well at the same temperature. Then, the latter solution was added suddenly over the $Pb(NO_3)_2$ under a slow stirring process leading to the deposition of PbS as a black precipitate. The latter was collected, washed, and dried at 60°C for 6 h. The schematic process of deposition of PbS on PANI is shown in Figure 1(a).

PANI/PbS nanocomposite was synthesized through the ionic surface adsorption process. The ATO/PANI was immersed in 0.05 M $Pb(NO_3)_2$ for 2 h at 298 K leading to the adsorption of Pb^{2+} over the PANI surface. The resulting ATO/PANI/Pb^{2+} composite film was dried and then immersed in (0.01 M) thiourea solution at 60°C for 15 min. The S^{2-} and Pb^{2+} ions reaction occurred, leading to ATO/PANI/PbS nanocomposite formation.

2.3. Characterization of the Prepared Nanomaterials. The crystal structure of PANI, PbS, and PANI/PbS was confirmed using X-ray diffraction (XRD), PANalytical Pro, Almelo, Netherlands, and Fourier transform infrared (FTIR)-Shimadzu 340 Jasco spectrophotometer, Easton, USA. The morphology of the samples was determined using scanning electron microscopy (SEM) ZEISS, Gemini, Oberkochen, Germany. The inside scanning was carried out using a transmission electron microscope (TEM) (JEOL JEM-2100, Waltham, USA). A simulation study for the SEM was carried out using the ImageJ program. The optical analyses were conducted using Shimadzu UV/Vis spectrophotometer (Perkin Elmer, Waltham, MA, USA).

2.4. The Electrochemical Test. The electrochemical study was carried out through a three-electrode cell using a power station (CHI660E), as shown in Figure 1(b). The prepared

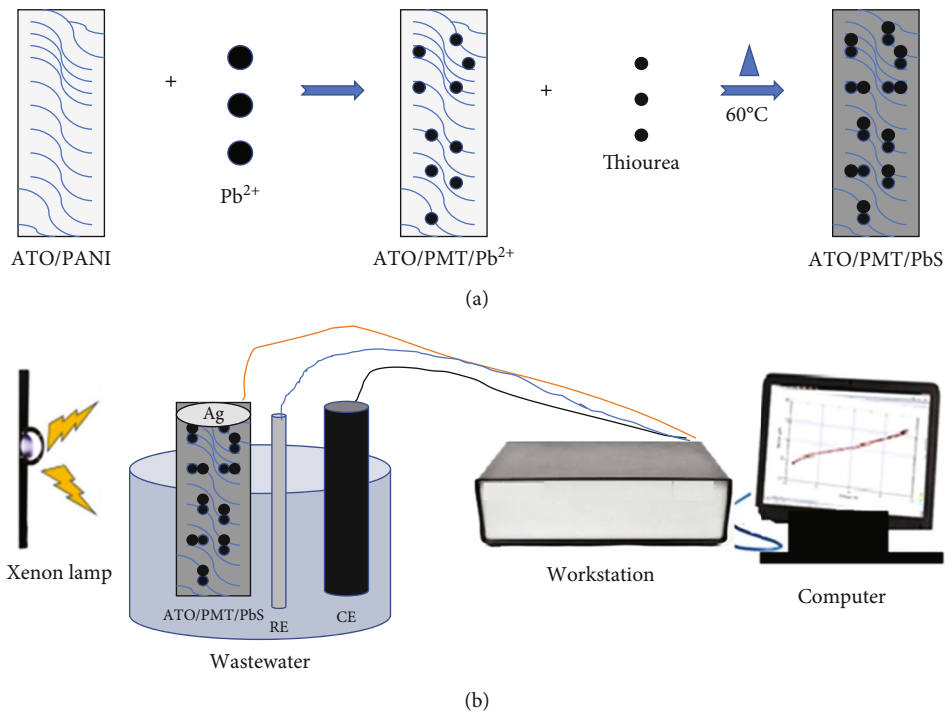

FIGURE 1: (a) The schematic deposition of PbS on ATO/PANI and (b) the three-electrode cell for electrochemical H_2 generation from wastewater.

ATO/PANI/PbS nanocomposite represented the working electrode, while the graphite and calomel were used as counter and reference electrodes, respectively. The measurements were carried out under a solar simulator device (xenon lamp), using sewage water as an electrolyte without any additional sacrificing agent.

3. Results and Discussion

3.1. Characterization of the Prepared Nanomaterials. The surface morphologies of PbS, PANI, and PANI/PbS were investigated by SEM analyses, as mentioned in Figures 2(a)–2(c). Figure 2(a) shows that the PbS has a random nonporous nature due to the aggregation of the nanoparticles.

The morphology of the prepared PANI thin film is shown in Figure 2(b), in which the prepared PANI has a porous network with an elongated particle shape. This porosity is further demonstrated in the magnified figure. Moreover, this porosity is the key to facilitating the PbS nanoparticles' penetration into the PANI network and deposition inside and outside the surface. This fact is confirmed in Figure 2(c), where the spherical PbS particles appear inside and outside the PANI network in the PANI/PbS material, having an average particle size of 43 nm.

The surface roughness and cross-section of PbS, PANI, and PANI/PbS thin films were studied using ImageJ software (Figures 2(d)–2(f). This morphological simulation strongly depends on the SEM real images. ImageJ confirms the nanoporous morphology of the PbS and PANI. Moreover, the composite PANI/PbS emerges with different nature, in which PbS white spheres coat the PANI network.

Furthermore, the TEM image of the PANI/PbS composite is shown in Figure 2(g) and 2(h) under different bare scales. The light and dark colors refer to the PANI and PbS nanoparticles inside the composite. The PbS nanoparticles are embedded with PANI nanoparticles with an interatomic distance of about 0.5 nm.

The abovementioned PANI/PbS composite morphology was expected to have a high-efficiency optical absorption behavior.

The FTIR spectra of PbS, PANI, and PANI/PbS nanomaterials are shown in Figure 3(a), and the corresponding summarized data is mentioned in Table 1. The vibration of the heteropolar PbS diatomic molecules appears at 1400 and 1601 cm^{-1}. The N-H, C-H, and C–N aromatic stretching vibrations for PANI occur at 3401, 2918, and 1105 cm^{-1}, respectively. The stretching vibrations of C=C quinoid and benzenoid rings appear at 1467 and 1301 cm^{-1}, respectively. The paradisubstituted aromatic rings appear at 587 cm^{-1}. After the PANI/PbS composite formation, there are redshifts for N-H, C=C quinoid, and C–N function groups stretching vibrations to 3424, 1470, and 1105 cm^{-1}, respectively. However, there is a blue shift for the C=C benzenoid ring to 1291 cm^{-1}.

The XRD diffractometers of PANI, PbS, and PANI/PbS nanomaterials are shown in Figure 3(b). For PANI (red line), there are three crystalline peaks at $2\theta = 15.1°$, 20.78°, and 25.55°, corresponding to the growth directions (011), (021), and (200), respectively.

For the PbS nanoparticles (black line), there are eight peaks, in which the three sharpest peaks appear at $2\theta =$ 25.98°, 30.17°, and 43.12° for the growth directions (110), (111), and (022), respectively. The other five peaks appear

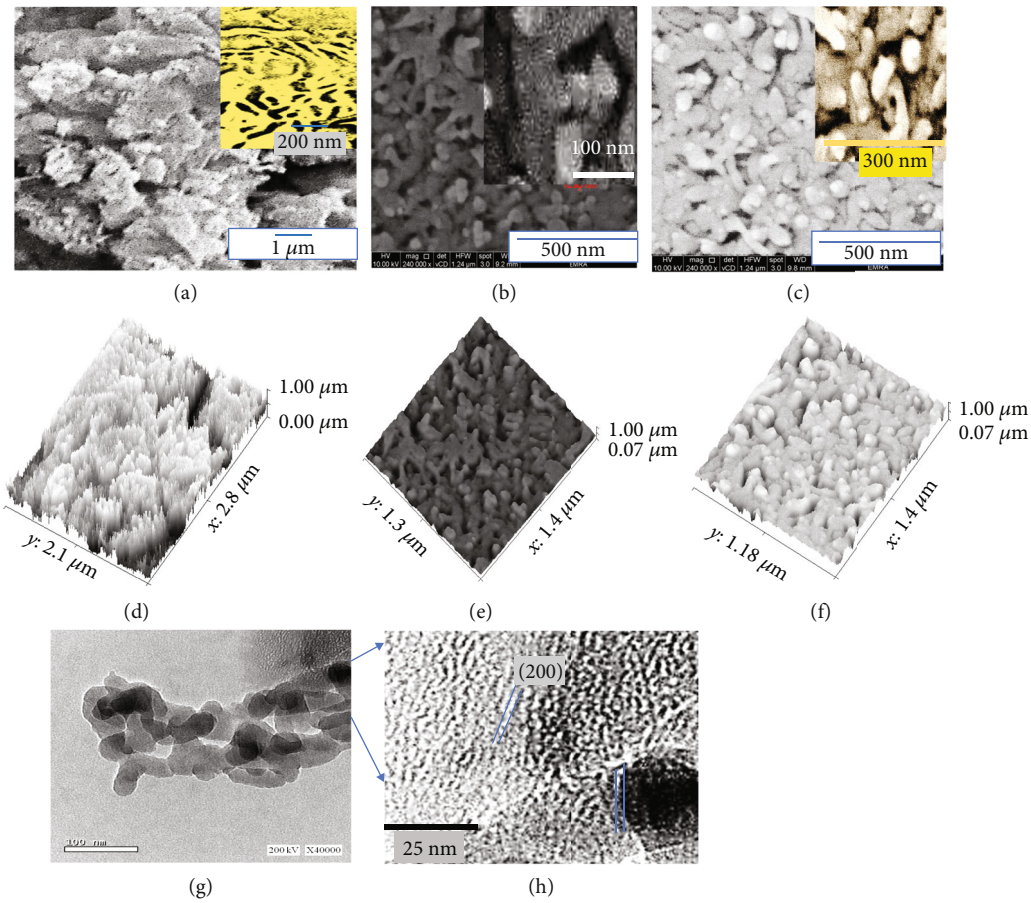

FIGURE 2: The SEM and modeling images of (a and d) PbS, (b and e) PANI, and (c and f) PANI/PbS nanomaterials. TEM images (g and h) for PANI/PbS nanocomposite at bare scales.

at 51.14°, 53.70°, 62.54, 68.82°, and 71.01° for the growth directions (132), (170), (222), (311), and (133), respectively.

After forming the PANI/PbS composite, there are shifts in the two PANI-related peaks to $2\theta = 25.49°$ and 33.6°, corresponding to (200) and (120), respectively. Moreover, nine additional peaks are noticed and can be assigned to the PbS nanoparticles incorporated in the composite; the three sharpest peaks at $2\theta = 26.55°$, 29.52°, and 53.62° correspond to the growth directions (110), (111), and (132), respectively. The other six peaks appear at $2\theta = 39.34°$, 43.63°, 50°, 74°, 61.95°, 64.50°, and 72.24° for the growth directions (120), (002), (022), (170), (222) (251), and (133), respectively.

The average crystal size of the nanocomposite equals 34 nm, calculated according to Scherrer's formula (Equation (1)) [35]. This equation depends on XRD wavelength (λ), Bragg angle (θ), dimensionless factor (k), and full width at half maximum (W).

$$D = \frac{0.9\lambda}{W} \cos\theta. \quad (1)$$

The application of the prepared ATO/PANI/PbS as photoelectrode for H_2 generation is based on its efficiency for light absorption. Therefore, an optical absorption study was conducted. The spectra of PANI, PbS, and PANI/PbS nanomaterials are given in Figure 3(c), while the bandgaps for these nanomaterials are shown in Figure 3(d). Regarding the PANI nanomaterial, there are three peaks at 275, 430, and 840 nm in the UV, Vis, and near IR, respectively. The sharpest two peaks in the UV and Vis regions correspond to the $\Pi - \Pi^*$ electron transition in the benzenoid ring. However, the peak in the near IR is assigned to the aromatic polymer conjugation. There are two peaks at 287 and 890 nm for the PbS nanoparticles in the UV and IR regions, respectively. The peaks in the IR region correlate with the dark color of the PbS nanoparticles that causes the vibrations of the electrons. The optical absorption behavior is enhanced after forming the PANI/PbS composite, especially in the Vis region with the highest intensity peak at 630 nm. Moreover, there is a redshift in the UV peak to 330 nm. This optical behavior indicates the composite's good light absorption efficiency compared to both PANI and PbS.

The bandgap (E_g) values of the prepared nanomaterials PANI, PbS, and PANI/PbS were calculated using Tauc's equation (Equations (2) and (3)). This equation is based on the absorbance (A), absorption coefficient (α), Planck constant (h), and frequency (ν) parameters. The bandgap relations are shown in Figure 3(d) for PANI, PbS, and PANI/PbS, in which the bandgap values are 2.5, 1.24, and

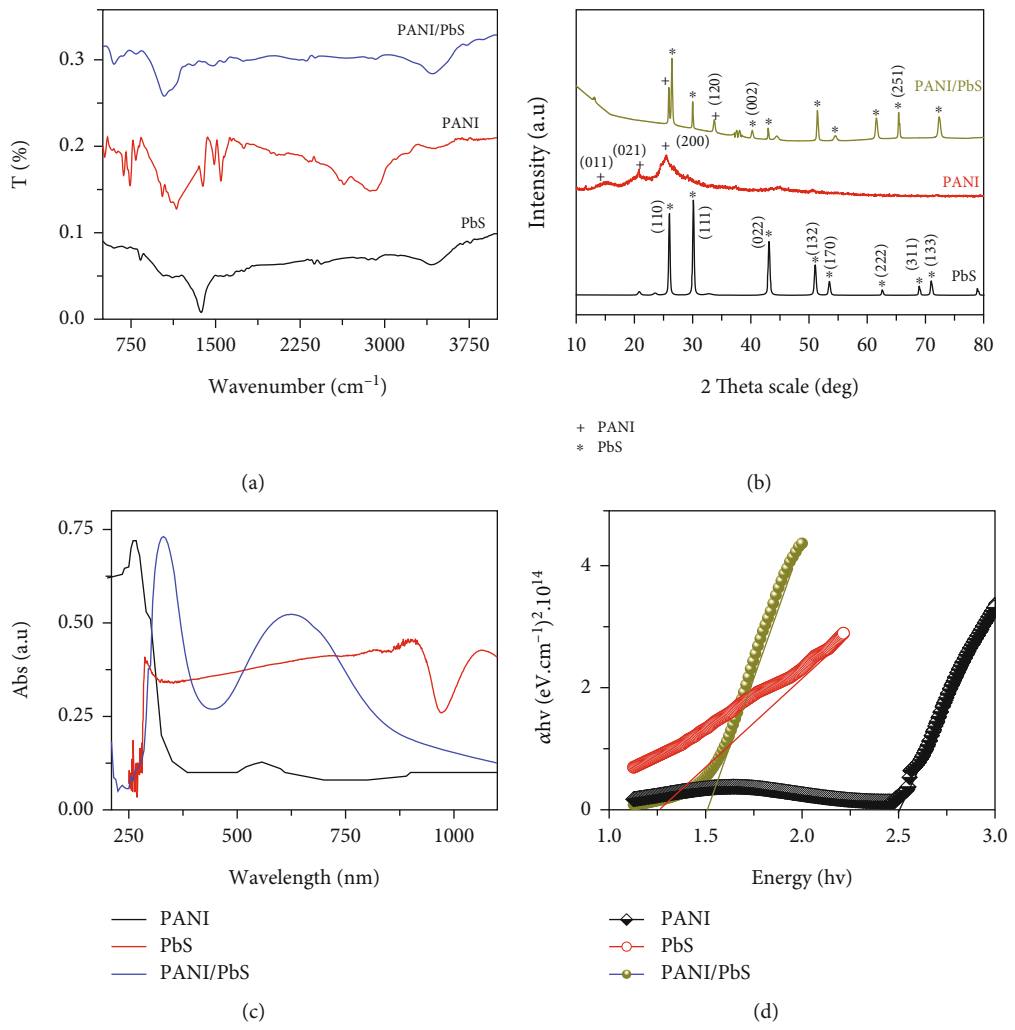

Figure 3: (a) FTIR, (b) XRD, (c) optical absorption, and (d) bandgap of PbS, PANI, and PANI/PbS nanomaterials.

Table 1: The FTIR data of PbS, PANI, and PANI/PbS nanomaterials.

Band position (cm^{-1})			Assignment
PANI/PbS	PANI	PbS	
3424	3401	—	N–H group [30]
2923 2856	2918	—	C-H aromatic ring group [31]
1470	1467	—	C=C of the quinoid ring [32]
1382	—	1400	Heteropolar diatomic molecules [20]
1291	1301	—	C=C of benzenoid rings [33]
1108	1105	—	C–N [34]
1043	1049	1061	Heteropolar diatomic molecules of PbS
792	789	—	C–H in-plane [34]
590	587	—	Paradisubstituted aromatic rings

1.5 eV, respectively. The PANI/PbS nanocomposite has the optimum bandgap value, so the optimum light absorption behavior was expected. This qualifies it for working as a photoelectrode for light absorption and then sewage water splitting for H_2 gas fuel generation.

$$\alpha h\nu = A\left(h\nu - E_g\right)^{1/2}, \tag{2}$$

$$\alpha = \left(\frac{2{,}303}{d}\right)A. \tag{3}$$

3.2. Photoelectrochemical Water Splitting. The photocatalytic wastewater-splitting reaction was achieved using a three-electrode cell, in which ATO/PANI/PbS, graphite sheet, and calomel are used as working, counter, and reference electrodes, respectively. The wastewater (third stage treatment), possessing a chemical composition mentioned in Table 2, was used as an electrolyte. At 25°C and a sweep rate of 100 mV.s^{-1}, the measurements were carried out using a workstation (CHI660E) under an artificial xenon lamp.

Under the light effect, there are significant changes in the produced current density (J_{ph}); the J_{ph} values increase from 10^{-8} to 0.13 mA.cm^{-2}, as shown in Figure 4(a). This behavior is confirmed in Figure 4(b), at a minimal bias voltage, in which the effect of on/off chopped light on the produced J_{ph} appears clearly. Under off light, the value of J_{ph} is almost zero, but under light irradiation, this value increases to 0.0018 mA.cm^{-2}. Considering curve 4(b), the stability of the electrode for water splitting is confirmed until 800 s. There are slight changes in J_{ph} values from 0.0018 to 0.0013 mA.cm^{-2}, with a time increase from 1.0 to 800 s. The high sensitivity of light can be correlated to the role of PbS, which help in light-capturing and trapping. The photons cause the generation of hot electrons that oscillate and localize on the surface. This PbS nanomaterial accepts additional electrons from PANI, which motivates the H_2O molecules to split to generate O_2 and H_2 gases.

The reproducibility of the PANI/PbS electrode is shown in Figure 4(c). The electrode has almost the same values under repeating runs. This confirms the stability of the prepared electrode for a water-splitting reaction. This stability is related to the PANI nature that does not dissolve in almost all chemical solvents.

The number of produced hydrogen moles was calculated by applying the Faradays law of electrolysis (Equation (4)) [36]. 0.1 mmol/cm^2 h of H_2 gas is delivered from the solution as bubbles. The Faradays law depends on many factors such as the J_{ph} value and change in time (Δt), taking into consideration the Faraday constant (F, 9.65×10^4 C.mol^{-1}), the molecular mass of hydrogen gas (M), and the oxidation number (z).

$$H_2(\text{moles}) = \int_0^t \frac{J_{ph}\,dt}{F} \cdot \frac{M}{z}. \quad (4)$$

The J_{ph} values of the ATO/PANI/PbS photoelectrode depend on the light intensity (photons number). By increasing the photons number, the photocatalytic materials will produce an increasing number of electrons reflected in the J_{ph} values. The photons number (N) is directly proportional to the light intensity (P), as shown in Equation (5), where (c) is the light velocity, (λ) is the wavelength, and (h) is the Planck constant. The photons activate the ATO/PANI/PbS nanocomposite active sites for electron-hole pair formation [37], which collects more electrons in the conducting band [38].

The relation between the light intensity (25 to 100 mW.cm^{-2}) and J_{ph} values is mentioned in Figures 5(a) and 5(b). The J_{ph} values increase from 0.1 to 0.13 mA.cm^{-2}, increasing the light intensity from 25 to 100 mW.cm^{-2}. Therefore, 100 mW.cm^{-2} has the optimum effect on the PANI/PbS photocatalytic materials due to the increasing number of photons per second that reach the electrode surface and cause electrons to oscillate and split water to generate H_2. These J_{ph} values represent the H_2 generation rate [31, 33].

Table 2: The wastewater chemical composition.

Material or element	Concentration (mg/L)
Phenols	0.015
F^-	1.0
Al^{3+}	3.0
NH_3	5.0
Hg^{2+}	0.005
Pb^{2+}	0.5
Cd^{3+}	0.05
As^{3+}	0.05
Cr^{3+}	1.0
Cu^{2+}	1.5
Ni^{3+}	0.1
Fe^{3+}	1.5
Mn^{2+}	1.0
Zn^{2+}	5.0
Ag^+	0.1
Ba^{3+}	2.0
Co^{2+}	2.0
Other cations	0.1
Pesticides	0.2
CN^-	0.1
Industrial washing	0.5
Coli groups	4000/100 cm^3

$$N = \frac{\lambda P}{hc}. \quad (5)$$

The effect of light wavelengths (390 to 636 nm) on the ATO/PANI/PbS photoelectrode is mentioned in Figure 6, in which the produced J_{ph} values are measured. It can be noticed that the photoelectrode responds well to the different light wavelengths. The J_{ph} values increase with decreasing the wavelength, and a 390-nm monochromatic light has an optimum J_{ph} value of 0.122 mA.cm^{-2}. Then, these values decrease until they reach 0.093 mA.cm^{-2} at 636 nm. The high J_{ph} value at 390 nm can be linked to the effect of high-energy UV monochromatic light that motivates the electrons to reach the conducting band of the nanocomposite. These hot electrons cause oscillation movements on the surface. This can be confirmed in Figure 6(b), where the wavelength and J_{ph} relation at +1 V is mentioned.

Based on these encouraging results, the prepared electrode responds to the different wavelengths in a broad light region.

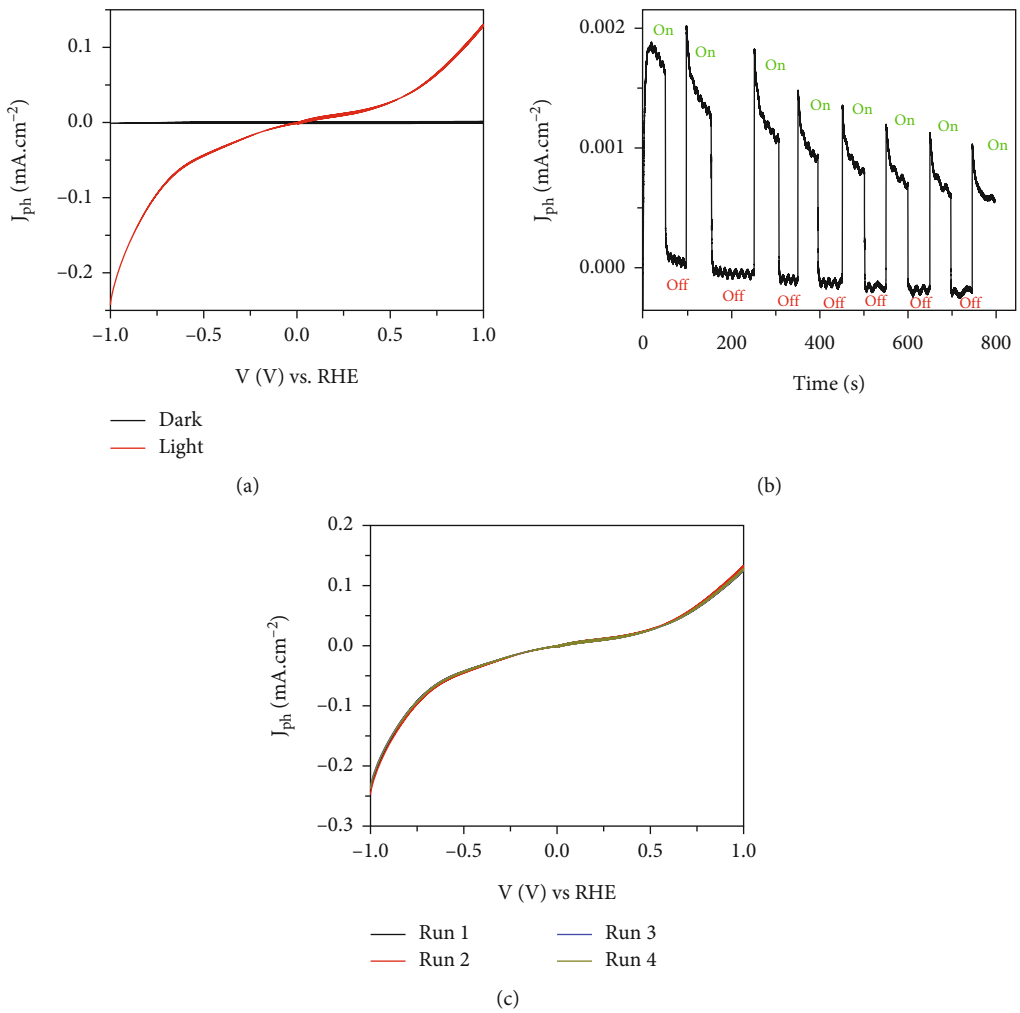

Figure 4: The effect of (a) dark and light, (b) on/off chopped light, and (c) reproducibility on the ATO/PANI/PbS photoelectrode.

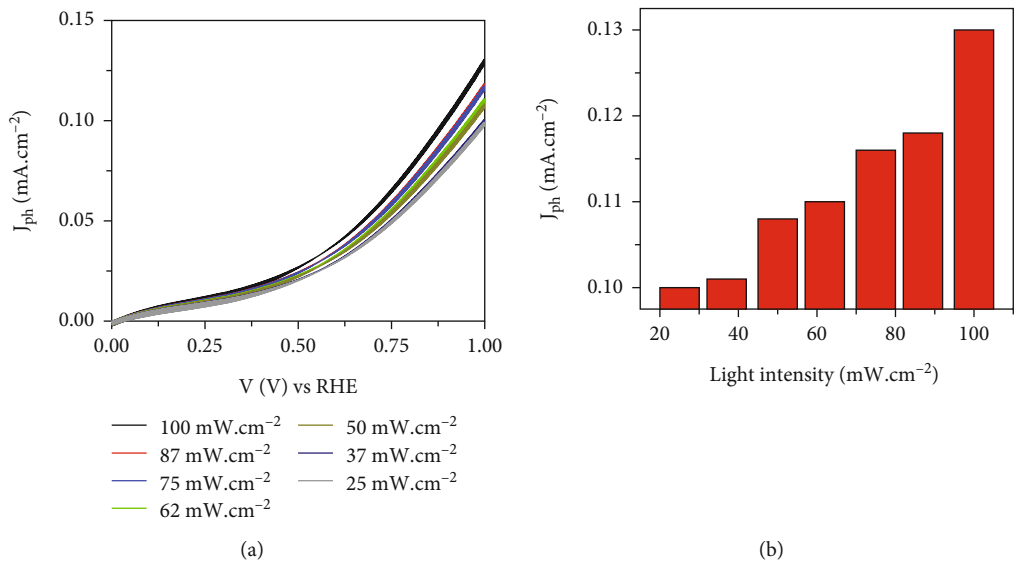

Figure 5: (a and b) The effect of light intensities on the ATO/PANI/PbS electrode for the current density values at 25°C.

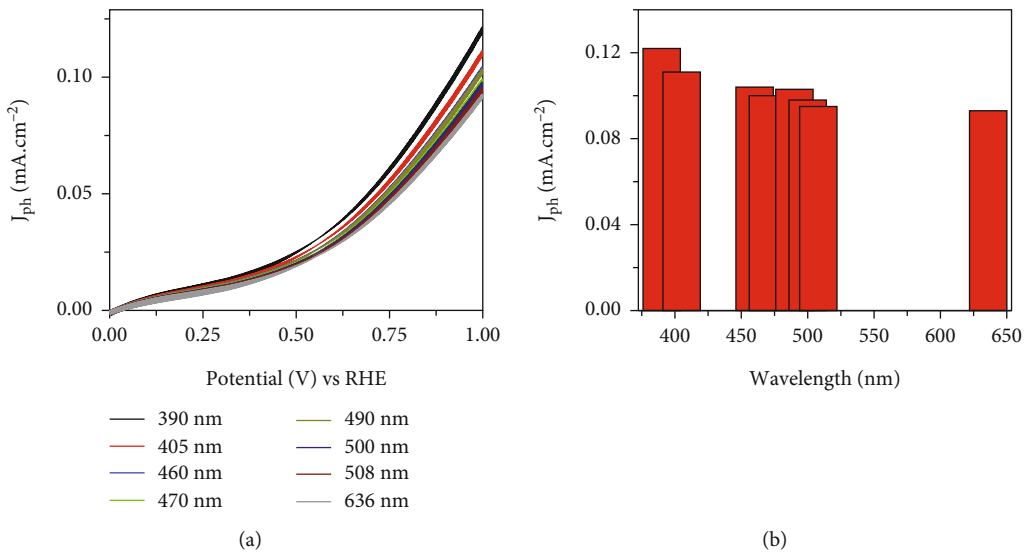

Figure 6: (a) The response of the ATO/PANI/PbS photoelectrode under different light wavelengths (390 to 636 nm) and (b) the J_{ph} values at +1 V for this photoelectrode at 25°C.

From 298 to 333 K, the effect of temperature on the ATO/PANI/PbS photoelectrode was studied, and the results are shown in Figures 7(a) and 7(b). This effect is reflected in the J_{ph} values that increase from 0.13 to 0.185 mA.cm^{-2}, increasing the temperature from 298 to 333 K. This increase can be assigned to the high mobility of ions that increases the electrons' transfer. Consequently, the water-splitting rate increases with increasing temperature, considering the J_{ph} values [39, 40]. Using Equation (6) and Figures 7(c) and 7(d), the thermodynamic parameters Ea, ΔS, and ΔH were determined. This calculation also depends on the h, k_B, R, and k, which correspond to Planck, Boltzmann, universal gas, and reaction rate constants. From the Eyring equation (Equation (6)) and Figure 7(c), the determined Ea value is 9.9 kJ/mol, while from Equation (6) and Figure 7(d), the determined ΔH^* and ΔS^* values are 7.3 kJ/mol and 273.4 J/mol.K, respectively. The small enthalpy obtained indicates the water splitting and H_2 generation that can easily occur. Moreover, the positive entropy value revealed confirms the reaction spontaneity.

A comparison of the used electrolytes and produced J_{ph} values in the literature with those in the current study was settled and summarized in Table 3. The prepared electrode has one of the highest J_{ph} values, indicating its high efficiency and light sensitivity. Also, the present work uses sewage water as an electrolyte without any additional sacrificing agent. In addition, the prepared electrode has a significant advantage in its high stability and reproducibility at a low cost. These advantages and properties can qualify the electrode for industrial applications.

Moreover, the H_2 moles are calculated from the Faraday equation (Equation (6)) [36], under time change (dt), using the Faraday constant (F). The estimated H_2 mole for the ATO/PANI/PbS photoelectrode is 38 μmol h^{-1} cm^{-2}.

$$H_2 \text{ mole} = \int_0^t J_{ph} \cdot \frac{dt}{F}. \quad (6)$$

3.3. Mechanism and Theoretical Study of H_2 Electrogeneration. The conversion of sewage water into H_2 gas is carried out through sequence electron transfer between the PANI and PbS nanomaterials. Under the light incidence, the PANI/PbS captures these photons, which are split into both levels of PANI and PbS. Consequently, the electrons are transferred from the valency band HOMO in PANI to the conducting band LUMO. Nevertheless, there is the additional electron transfer from LUMO in PANI to the PbS conduction band having a lower energy level. Finally, the accumulated electrons on the PbS surface are directly transferred to the neighbor wastewater used as an initiator for the splitting process. Due to the difference in the energy levels of PANI and PbS, the Schottky barrier is formed, disrupting the electron transfer. This appears in the behavior of the current-voltage curve Figure 4(a) or 4(c). The role of PbS is crucial in minimizing the bandgap for the whole composite to reach 1.5 eV, which is close to the ideal bandgap of 1.2 to 1.3 eV. In addition, PbS has a dark color that captures and absorbs the light well, in which the photons reach the PANI surface. The role of PANI in the composite is also crucial, and it is the main material that has high compact to the supporting material ATO with high corrosion resistance and high lifetime. The main disadvantage of PANI is its large bandgap of about 2.5 eV, noting that this bandgap is enhanced using the PbS nanomaterial.

Figure 8(a) shows the nudged elastic band (NEB) [47] calculation of the energies along with the reaction path towards the production of hydrogen from water and PANI/PbS. We employed the NEB in the atomic simulation environment (ASE) [48]. The structure energy and minimization were performed via the xtb tight-binding module [49] and the BFGC method [50], respectively. We used the default module settings for the convergence thresholds and other calculation parameters.

The calculated reaction barrier is ΔE ~7 eV (this is one order of magnitude higher than 1 eV due to the nature of the

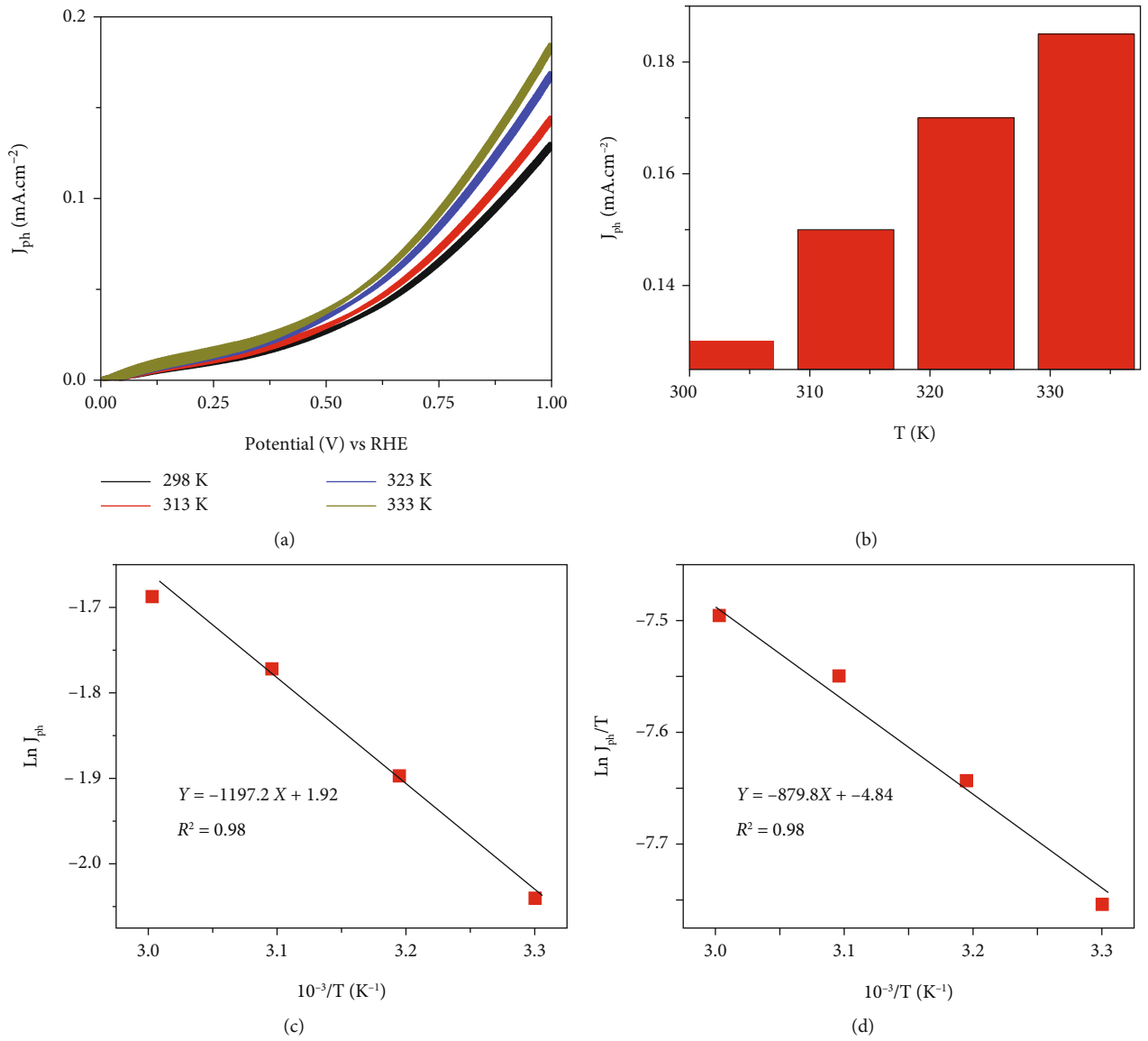

Figure 7: (a and b) The temperature effect on ATO/PANI/PbS. The relations between (c) temperature reciprocal and LnJ_{ph} and (d) temperature reciprocal and LnJ_{ph}/T.

Table 3: Comparison of the electrolytes and J_{ph} values of the prepared photoelectrode with literature studies.

Photoelectrode	Electrolyte	Voltage bias (V)	Jph (mA/cm^2)
Ni/PANI [22]	H_2SO_4	0.45	0.0012
Poly(3-aminobenzoic acid) frame [41]	H_2SO_4	1.2	0.08
g-C_3N_4-CuO [42]	NaOH	1.1	0.01
CuO-C/TiO_2 [43]	Glycerol	0.5	0.012
Au/TiO_2 [41]	NaOH	1.2	3.0×10^{-4}
$BiFeO_3$ [44]	NaOH	1.2	0.1
Au/Pb(Zr, Ti)O_3 [45]	NaOH	1.1	0.06
PrFeO [46]	Na_2SO_4	1.0	0.129
Fe_2O_3	NaOH	1.23	0.003
ATO/PANI/PbS (present work)	Sewage water	1.0	0.13

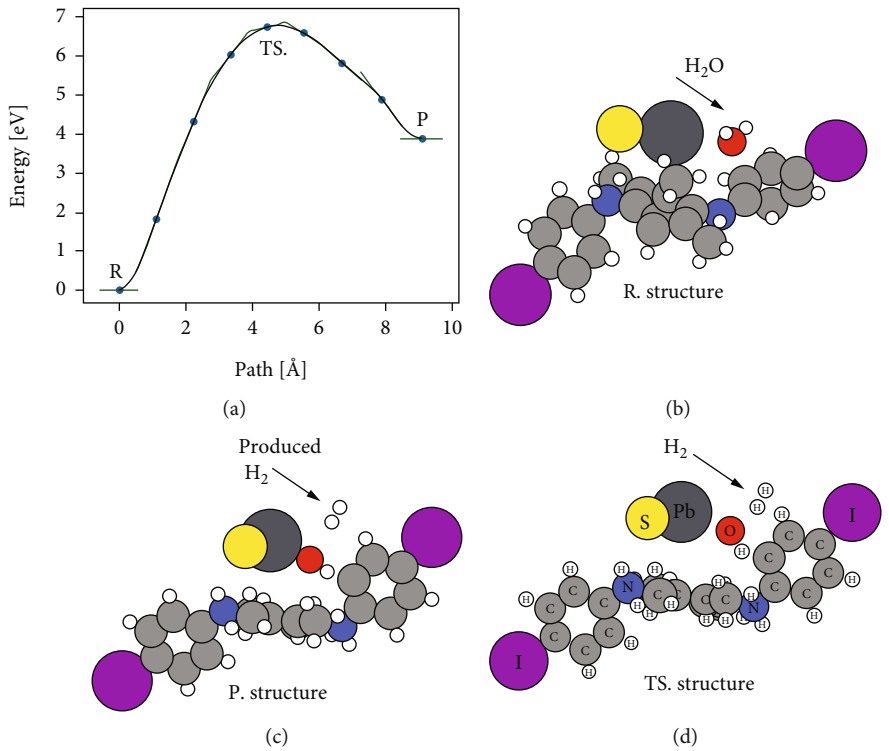

Figure 8: (a) The nudged elastic band (NEB) calculation of the energies along the reaction path towards hydrogen production. ΔE ~7 eV is the reaction path barrier. (b) The structure of the water and PANI/PbS reactants (R). (c) The product structure (P) after the splitting of the hydrogen. (d) The transition state structure (TS).

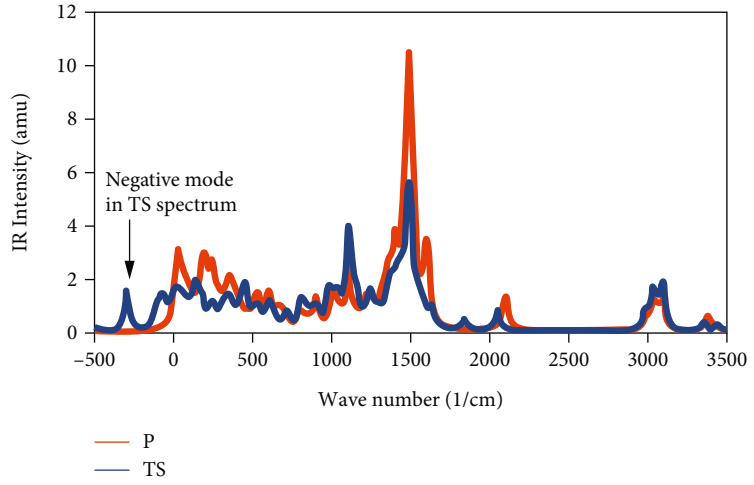

Figure 9: The calculated infrared (IR) spectrum for the P (orange line) and TS (blue line).

qualitative method used for the calculation), which separates the reactant (R, Figure 8(b) and product (P, Figure 8(c)). Overcoming this barrier by the reactant leads to the production of the H_2, as shown in Figure 8(c). Figure 8(d) shows the structure of the transition state (TS). The metastability [10] of this TS state is verified from the negative infrared (IR) frequencies (or wavenumbers (~ -250 cm^{-1})) as shown in the IR spectrum of the TS in Figure 9 (blue line). On the contrary, the stability of the P is evident from the absence of negative frequency modes in its IR spectrum (orange line, Figure 9). The R is also stable; however, we do not show its IR spectrum to avoid crowding the space in Figure 9. The IR peaks are expected to be dominated by the vibrations of the bonds in the PANI/PbS.

Besides the IR spectra in Figure 9, thermochemistry calculations gave rise to the $\Delta G(\text{TS} \longrightarrow R) = -7$ kcal/mol and $\Delta G(\text{TS} \longrightarrow P) = -2$ kcal/mol, representing the changes in the calculated free energies in the reaction path from the

Table 4: The nomenclature and its definition of the items used in the present theoretical and experimental study.

Nomenclature	Definition
Tight-binding method	A computationally fast, semiempirical method for solving Bloch states of a material
Transition state	A particular unstable chemical configuration along the reactant-to-product reaction path
IR	A spectroscopic method utilizing infrared electromagnetic radiation to excite the harmonic vibrations of molecules
SEM	Scanning electron microscope
TEM	Transmission electron microscope
XRD	X-ray diffraction
J_{ph}	Current density (light)
J_O	Current density (dark)
R	Photoresponsivity
D	Detectivity

Table 5: The input and output parameters used in the present theoretical and experimental study.

Input main parameters	Output main parameters
Theoretical study (1) Reactant *xyz* optimized atomic positions (2) Product *xyz* atomic positions (3) Number of images (configurations) in the reaction path (5 in our case) (4) Interatomic force threshold used in conjunction with the Broyden, Fletcher, Goldfarb, and Shanno (or BFGS) local search optimization algorithm (5) Temperature required for IR frequency calculations (298 K)	Reaction path (energy vs. position) IR spectrum
Experimental study (1) Potential -1.0 to +1.0 V (2) Scan rate 100 mV.s^{-1} (3) Three-electrode cell (4) Wastewater electrolyte	H_2 gas with 38 μmol h^{-1} cm^{-2}

reactant to the TS and from TS to the product, respectively. The $\Delta G(\text{TS} \longrightarrow R) < \Delta G(\text{TS} \longrightarrow P)$ indicates the possibility of the reformation (i.e., the reverse reaction from TS to R) of the reactant with a fraction slightly higher than that for the product. Nevertheless, the calculation demonstrates the successful production of H_2 in a water-splitting reaction catalyzed by PANI/PbS.

It is worth stressing that the calculation of Figure 8 gives a qualitative result about the reaction path. Quantitative reaction path analysis for comparison with experiments is possible by implementing the more computationally expensive quantum density functional methods. However, our present qualitative result clearly shows the formation of the reaction barrier in the path toward splitting the hydrogen from the water catalyzed by the PbS-polyaniline.

Finally, the nomenclature and its definition are mentioned in Table 4, while the input and output parameters are mentioned in Table 5.

4. Conclusions

Sewage water was valorized, and ATO/PANI/PbS nanocomposite was prepared and used as a photocathode for H_2 production. The preparation process was carried out using the polymer to assist the PbS deposition in two steps: Pb^{2+} adsorption and then PbS deposition using thiourea and heating. The prepared nanocomposite was characterized using multiple techniques such as SEM, TEM, XRD, FTIR, and UV/Vis absorption. The FTIR and XRD analyses confirmed the chemical structure of PANI, PbS, and PANI/PbS composite. The latest's average crystal size was 34 nm, determined by XRD.

The TEM, SEM, and ImageJ software confirmed the morphology of the PANI, PbS, and PANI/PbS, where PANI had a porous network nature making it an excellent candidate for the deposition of PbS in its pores and on its surface with high contact. Moreover, the bandgap of the composite, 1.5 eV, was more preferred than the solo PANI or PbS bandgaps of 2.5 and 1.24 eV, respectively. The conversion of the sewage water into H_2 gas fuel was carried out through the prepared electrode with high efficiency. The electrode responded well to light, where the current density changed from 10^{-8} to 0.13 mA.cm^{-2} under dark and light, respectively. The thermodynamic parameters ΔH^* and ΔS^* were 7.3 kJ/mol and 273.4 J/mol.K, respectively. Finally, the mechanism explains the H_2 generation reaction using three-electrode cell.

Our team is working on synthesizing a prototype that can valorize and directly convert the wastewater into hydrogen fuel. The cost of producing 200 ml of hydrogen is about 2$. Our perspective is to decrease this cost to 1$ for one liter of hydrogen gas.

Data Availability

All the data used to support the findings of this study are included within the article.

Conflicts of Interest

The authors declare no conflict of interest.

Acknowledgments

The authors extend their appreciation to the Deanship of Scientific Research at Al Jouf University for funding this work through a research grant (no. DSR-2021-03-0314).

References

[1] H. Nishiyama, T. Yamada, M. Nakabayashi et al., "Photocatalytic solar hydrogen production from water on a $^{100\text{-m2}}$ scale," *Nature*, vol. 598, no. 7880, pp. 304–307, 2021.

[2] T. Hisatomi and K. Domen, "Reaction systems for solar hydrogen production via water splitting with particulate semiconductor photocatalysts," *Nature Catalysis*, vol. 2, no. 5, pp. 387–399, 2019.

[3] M. Pagliaro, "Preparing for the future: solar energy and bioeconomy in the United Arab Emirates," *Energy Science & Engineering*, vol. 7, no. 5, pp. 1451–1457, 2019.

[4] T. Takata, J. Jiang, Y. Sakata et al., "Photocatalytic water splitting with a quantum efficiency of almost unity," *Nature*, vol. 581, no. 7809, pp. 411–414, 2020.

[5] F. Mohamed, M. Rabia, and M. Shaban, "Synthesis and characterization of biogenic iron oxides of different nanomorphologies from pomegranate peels for efficient solar hydrogen production," *Journal of Materials Research and Technology*, vol. 9, no. 3, pp. 4255–4271, 2020.

[6] M. Shaban, S. Ali, and M. Rabia, "Design and application of nanoporous graphene oxide film for CO_2, H_2, and C_2H_2 gases sensing," *Journal of Materials Research and Technology*, vol. 8, no. 5, 2019.

[7] A. M. A. A. M. Elsayed, M. Rabia, M. Shaban, A. H. Aly, and A. M. Ahmed, "Preparation of hexagonal nanoporous Al_2O_3/TiO_2/TiN as a novel photodetector with high efficiency," *Scientific Reports*, vol. 11, no. 1, p. 17572, 2021.

[8] Z. Kang, Y. Cheng, Z. Zheng et al., "MoS_2-based photodetectors powered by asymmetric contact structure with large work function difference," *Nano-Micro Letters*, vol. 11, no. 1, pp. 12–34, 2019.

[9] J. H. Lee, W. W. Lee, D. W. Yang, W. J. Chang, S. S. Kwon, and W. Il Park, "Anomalous photovoltaic response of graphene-on-GaN Schottky photodiodes," *ACS Applied Materials and Interfaces*, vol. 10, no. 16, pp. 14170–14174, 2018.

[10] K. B. Bec and C. W. Huck, "Advances in near-infrared spectroscopy and related computational methods," *Molecules*, vol. 24, no. 23, p. 4370, 2019.

[11] Q. M. Koh, C. G. Tang, M. C. Ang et al., "Overcoming the water oxidative limit for ultra-high-workfunction hole-doped polymers," *Nature Communications*, vol. 12, no. 1, pp. 1–10, 2021.

[12] J. Chen, W. Huang, D. Zheng et al., "Highly stretchable organic electrochemical transistors with strain-resistant performance," *Nature Materials*, vol. 21, no. 5, pp. 564–571, 2022.

[13] Q. Zhang, H. Parimoo, E. Martel, and S. Zhao, "Vertical semiconductor deep ultraviolet light emitting diodes on a nanowire- assisted aluminum nitride buffer layer," *Scientific Reports*, vol. 12, no. 1, pp. 1–7, 2022.

[14] C. Yuan, Y. Zhou, Y. Zhu et al., "Polymer/molecular semiconductor all-organic composites for high-temperature dielectric energy storage," *Nature Communications*, vol. 11, no. 1, pp. 1–8, 2020.

[15] D. Kim, D. Ndaya, R. Bosire et al., "Dynamic magnetic field alignment and polarized emission of semiconductor nanoplatelets in a liquid crystal polymer," *Nature Communications*, vol. 13, no. 1, pp. 1–10, 2022.

[16] A. A. A. Abdelazeez, N. M. A. Hadia, A.-H. I. Mourad et al., "Effect of Au plasmonic material on poly M-toluidine for photoelectrochemical hydrogen generation from sewage water," *Polymers*, vol. 14, no. 4, 2022.

[17] M. Shaban, M. Rabia, W. Fathallah et al., "Preparation and characterization of polyaniline and Ag/polyaniline composite nanoporous particles and their antimicrobial activities," *Journal of Polymers and the Environment*, vol. 26, no. 2, pp. 434–442, 2018.

[18] M. R. Abukhadra, M. Rabia, M. Shaban, and F. Verpoort, "Heulandite/polyaniline hybrid composite for efficient removal of acidic dye from water; kinetic, equilibrium studies and statistical optimization," *Advanced Powder Technology*, vol. 29, no. 10, pp. 2501–2511, 2018.

[19] M. Shaban, M. R. Abukhadra, M. Rabia, Y. A. Elkader, and M. R. Abd El-Halim, "Investigation the adsorption properties of graphene oxide and polyaniline nano/micro structures for efficient removal of toxic Cr(VI) contaminants from aqueous solutions; kinetic and equilibrium studies," *Rendiconti Lincei*, vol. 29, no. 1, pp. 141–154, 2018.

[20] M. Shaban, M. Rabia, A. M. A. El-Sayed, A. Ahmed, and S. Sayed, "Photocatalytic properties of PbS/graphene oxide/polyaniline electrode for hydrogen generation," *Scientific Reports*, vol. 7, no. 1, article 14100, 2017.

[21] M. Rabia, H. S. H. Mohamed, M. Shaban, and S. Taha, "Preparation of polyaniline/PbS core-shell nano/microcomposite and its application for photocatalytic H_2 electrogeneration from H_2O," *Scientific Reports*, vol. 8, no. 1, 2018.

[22] D. A. Dalla Corte, C. Torres, P. D. S. Correa, E. S. Rieder, and C. D. F. Malfatti, "The hydrogen evolution reaction on nickel-polyaniline composite electrodes," *International Journal of Hydrogen Energy*, vol. 37, no. 4, pp. 3025–3032, 2012.

[23] C. Belabed, A. Abdi, Z. Benabdelghani, G. Rekhila, A. Etxeberria, and M. Trari, "Photoelectrochemical properties of doped polyaniline: application to hydrogen photoproduction," *International Journal of Hydrogen Energy*, vol. 38, no. 16, pp. 6593–6599, 2013.

[24] N. Zhang, W. Ma, T. Wu, H. Wang, D. Han, and L. Niu, "Edge-rich MoS_2 naonosheets rooting into polyaniline nanofibers as effective catalyst for electrochemical hydrogen evolution," *Electrochimica Acta*, vol. 180, pp. 155–163, 2015.

[25] G. F. Teixeira, E. Silva Junior, R. Vilela, M. A. Zaghete, and F. Colmati, "Perovskite structure associated with precious metals: influence on heterogenous catalytic process," *Catalysts*, vol. 9, no. 9, p. 721, 2019.

[26] M. Mishra and D. M. Chun, "α-Fe_2O_3 as a photocatalytic material: a review," *Applied Catalysis A: General*, vol. 498, pp. 126–141, 2015.

[27] C. Acar, I. Dincer, and G. F. Naterer, "Review of photocatalytic water-splitting methods for sustainable hydrogen production,"

International Journal of Energy Research, vol. 40, no. 11, pp. 1449–1473, 2016.

[28] C. Y. Chiang, K. Aroh, N. Franson, V. R. Satsangi, S. Dass, and S. Ehrman, "Copper oxide nanoparticle made by flame spray pyrolysis for photoelectrochemical water splitting - Part II. Photoelectrochemical study," *International Journal of Hydrogen Energy*, vol. 36, no. 24, pp. 15519–15526, 2011.

[29] X. Guo, P. Diao, D. Xu et al., "CuO/Pd composite photocathodes for photoelectrochemical hydrogen evolution reaction," *International Journal of Hydrogen Energy*, vol. 39, no. 15, pp. 7686–7696, 2014.

[30] S. M. Sayyah, M. Shaban, and M. Rabia, "m-Toluidine polymer film coated platinum electrode as a pH sensor by potentiometric methods," *Sensor Letters*, vol. 13, no. 11, pp. 961–966, 2015.

[31] S. M. Sayyah, M. Shaban, and M. Rabia, "Electropolymerization of m-toluidin on platinum electrode from aqueous acidic solution and character of the obtained polymer," *Advances in Polymer Technology*, vol. 37, no. 1, p. 136, 2018.

[32] S. M. Sayyah, M. Shaban, and M. Rabia, "A sensor of m-toluidine/m-cresol polymer film for detection of lead ions by potentiometric methods," *Sensor Letters*, vol. 14, no. 5, 2016.

[33] S. M. Sayyah, M. Shaban, and M. Rabia, "A high-sensitivity potentiometric mercuric ion sensor based on m-toluidine films," *IEEE Sensors Journal*, vol. 16, no. 6, pp. 1541–1548, 2016.

[34] E. S. M. Sayyah, M. Shaban, and M. Rabia, "A sensor of m-cresol nanopolymer/Pt-electrode film for detection of lead ions by potentiometric methods," *Advances in Polymer Technology*, vol. 37, no. 5, p. 1304, 2018.

[35] A. M. Ahmed, M. Rabia, and M. Shaban, "The structure and photoelectrochemical activity of Cr-doped PbS thin films grown by chemical bath deposition," *RSC Advances*, vol. 10, no. 24, pp. 14458–14470, 2020.

[36] A. Almohammedi, M. Shaban, H. Mostafa, and M. Rabia, "Nanoporous TiN/TiO_2/alumina membrane for photoelectrochemical hydrogen production from sewage water," *Nanomaterials*, vol. 11, no. 10, p. 2617, 2021.

[37] L. Yang and Z. Liu, "Study on light intensity in the process of photocatalytic degradation of indoor gaseous formaldehyde for saving energy," *Energy Conversion and Management*, vol. 48, no. 3, pp. 882–889, 2007.

[38] E. Baniasadi, I. Dincer, and G. F. Naterer, "Measured effects of light intensity and catalyst concentration on photocatalytic hydrogen and oxygen production with zinc sulfide suspensions," *International Journal of Hydrogen Energy*, vol. 38, no. 22, pp. 9158–9168, 2013.

[39] M. S. S. Fadel, M. Rabia, S. Ezzat, N. Mansour, E. Saeed, and S. M. Sayyah, "Effect of annealing temperature on VO_2(M)/ITO film nanomaterials for thermochromic smart windows application and study its contact angle," *Journal of Nanophotonics*, vol. 12, no. 1, article 016009, 2018.

[40] M. Rabia, M. Shaban, B. M. Jibali, and A. A. Abdelkhaliek, "Effect of annealing temperature on the photoactivity of ITO/VO2(M)/Au film electrodes for water splitting," *Journal of Nanoscience and Nanotechnology*, vol. 20, no. 7, pp. 4120–4130, 2020.

[41] A. Naldoni, U. Guler, Z. Wang et al., "Broadband hot-electron collection for solar water splitting with plasmonic titanium nitride," *Advanced Optical Materials*, vol. 5, no. 15, article 1601031, 2017.

[42] V. Ragupathi, M. A. Raja, P. Panigrahi, and N. Ganapathi Subramaniam, "CuO/g-C_3N_4 nanocomposite as promising photocatalyst for photoelectrochemical water splitting," *Optik*, vol. 208, article 164569, 2020.

[43] X. Huang, M. Zhang, R. Sun, G. Long, Y. Liu, and W. Zhao, "Enhanced hydrogen evolution from CuOx-C/TiO_2 with multiple electron transport pathways," *PLoS One*, vol. 14, no. 4, article e0215339, 2019.

[44] G. Liu, S. K. Karuturi, H. Chen et al., "Enhancement of the photoelectrochemical water splitting by perovskite $BiFeO_3$*via* interfacial engineering," *Solar Energy*, vol. 202, pp. 198–203, 2020.

[45] Z. Wang, D. Cao, L. Wen et al., "Manipulation of charge transfer and transport in plasmonic-ferroelectric hybrids for photoelectrochemical applications," *Nature Communications*, vol. 7, no. 1, pp. 1–8, 2016.

[46] E. Freeman, S. Kumar, S. R. Thomas, H. Pickering, D. J. Fermin, and S. Eslava, "PrFeO3 photocathodes prepared through spray pyrolysis," *ChemElectroChem*, vol. 7, no. 6, pp. 1365–1372, 2020.

[47] H. Jónsson, G. Mills, and K. W. Jacobsen, *Nudged elastic band method for finding minimum energy paths of transitions*, Citeseer, 1998.

[48] A. H. Larsen, L. J. Mortensen, J. Blomqvist et al., "The atomic simulation environment—a Python library for working with atoms," *Journal of Physics: Condensed Matter*, vol. 29, no. 27, article 273002, 2017.

[49] C. Bannwarth, S. Ehlert, and S. Grimme, "GFN2-xTB—an accurate and broadly parametrized self-consistent tight-binding quantum chemical method with multipole electrostatics and density-dependent dispersion contributions," *Journal of Chemical Theory and Computation*, vol. 15, no. 3, pp. 1652–1671, 2019.

[50] D. Sheppard, R. Terrell, and G. Henkelman, "Optimization methods for finding minimum energy paths," *The Journal of Chemical Physics*, vol. 128, no. 13, article 134106, 2008.